

Diverging Flows: Detecting Extrapolations in Conditional Generation

Constantinos Tsakonas¹ Serena Ivaldi¹ Jean-Baptiste Mouret¹

Abstract

The ability of Flow Matching (FM) to model complex conditional distributions has established it as the state-of-the-art for prediction tasks (e.g., robotics, weather forecasting). However, deployment in safety-critical settings is hindered by a critical extrapolation hazard: driven by smoothness biases, flow models yield plausible outputs even for off-manifold conditions, resulting in silent failures indistinguishable from valid predictions. In this work, we introduce *Diverging Flows*, a novel approach that enables a single model to simultaneously perform conditional generation and native extrapolation detection by structurally enforcing inefficient transport for off-manifold inputs. We evaluate our method on synthetic manifolds, cross-domain style transfer, and weather temperature forecasting, demonstrating that it achieves effective detection of extrapolations without compromising predictive fidelity or inference latency. These results establish *Diverging Flows* as a robust solution for trustworthy flow models, paving the way for reliable deployment in domains such as medicine, robotics, and climate science.

1. Introduction

Conditional generative models have transcended their initial successes in media synthesis to become effective tools for probabilistic regression in scientific discovery and decision-making. Unlike traditional deterministic regression, which outputs a single mean prediction, these models learn the full conditional density $p(y|x)$ mapping complex inputs to high-dimensional target states. While Diffusion models initially drove this wave (Sohl-Dickstein et al., 2015; Ho et al., 2020), Flow Matching (FM) (Lipman et al., 2022; Tong et al., 2023) has emerged as a superior alternative for physical modeling. Crucially, whereas Diffusion models induce complex,

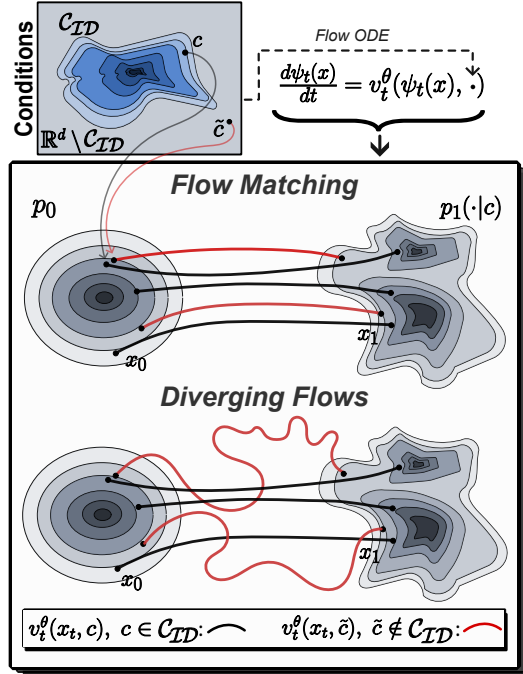


Figure 1. Conceptual overview of Diverging Flows. (Top) Flow Matching minimizes transport cost everywhere, forcing off-manifold inputs (red) to converge silently. (Bottom) Diverging Flows breaks this symmetry by enforcing transport inefficiency for invalid conditions. This ensures valid conditions (c) induce optimal flows, while off-manifold inputs (\tilde{c}) trigger detectable divergence.

curved trajectories due to their underlying noise schedules, Optimal Transport FM (OT-FM) explicitly optimizes for straight-line, constant-velocity paths. This makes OT-FM more computationally efficient and numerically stable than Diffusion, providing the precise, high-fidelity control required in critical domains such as robotics (Chi et al., 2023; Black et al., 2024; Rouxel et al., 2024; 2025) and climate forecasting (Chen & Lipman, 2024).

However, a fundamental limitation of these models is their lack of transparency. It is a core requirement of responsible AI that models should not be trusted on inputs for which they were not trained (Cao & Yousefzadeh, 2023). Yet, FM models inherently violate this principle. Driven by strong inductive biases towards smoothness and generalization (Rahaman et al., 2019), they tend to fail silently when queried with off-manifold conditions.

¹Inria, Université de Lorraine, CNRS, Loria, F-54000. Correspondence to: Constantinos Tsakonas <constantinos.tsakonas@inria.fr>.

Rather than signaling uncertainty, these models extrapolate, generating plausible-looking outputs even for physically impossible or semantically meaningless inputs. Additionally, standard likelihood-based safety checks are ineffective, due to the “likelihood paradox” where models assign high confidence to simple off-manifold inputs (Nalisnick et al., 2018; Serrà et al., 2019). While such hallucination is a feature in creative synthesis (Mariani et al., 2024; Guerreiro et al., 2024; Kim et al., 2024; Ki et al., 2025), in scientific and industrial domains, knowing whether a model has extrapolated is a fundamental requirement for transparency and accountability (Herrera-Poyatos et al., 2025). Without this mechanism, high-stakes deployment remains dangerous (Price et al., 2025; Rouxel et al., 2024).

To understand the critical role of these models as regressors, consider an autonomous energy grid relying on generative model for weather forecasts to balance load. In this setting, the model’s greatest strength, its ability model a complex conditional distribution, becomes its most dangerous property. If a satellite sensor malfunctions and feeds the model thermodynamically impossible data, a standard FM model will not fail visibly. Instead, it will silently hallucinate a coherent, high-resolution storm front to reconcile the glitch. The grid control system, receiving a technically valid forecast, might trigger emergency measures based on a phantom event. Hence, in high-stakes regression, the capacity to reject an invalid input is as critical as the capacity to predict a future one.

Addressing this effectively is difficult because the source of the error is the model’s own capabilities to create a smooth flow. Modern backbones (e.g., Transformers, U-Nets) are so effective at generalizing that they can find a smooth path between almost any arbitrary input and output. Existing solutions often rely on training separate classifiers or One-Class Classifiers (Cui et al., 2023; Chalapathy & Chawla, 2019), doubling the computational cost. Others rely on explicit outlier exposure (Hendrycks et al., 2018), which requires a representative dataset of “unknowns”, an assumption that requires knowing what you do not know.

Regarding OT-FM, we believe that the solution for that problem lies in the geometry of the generative process. We hypothesize that an FM model should exhibit a *geometric phase transition*: valid conditions must induce optimal transport, while off-manifold queries should trigger a breakdown in the vector field. This structural divergence transforms detection from a statistical problem into a geometric constraint, allowing the model to signal its limits via path turbulence. Closely related to the standard out-of-distribution (OOD) detection, this re-frames the problem as conservative distribution learning (Ma et al., 2021; Shao et al., 2024; Lubold & Taylor, 2022). To this end, our core contribution is a unified framework that enables a **single Flow Matching**

model to perform **high-fidelity** prediction while **detecting extrapolations**, eliminating the need for external models.

2. Related Work

2.1. Generative Models for Predictive Tasks

In robotics, Flow Matching and Diffusion models have become a successful alternative for visuomotor control policies, learning to map sensory observations to precise action trajectories (Chi et al., 2023; Black et al., 2024; Rouxel et al., 2024). Additionally, in computational biology, these models have been successfully applied to protein backbone design, regressing 3D molecular structures from sequence conditioning (Jing et al., 2023; Bose et al., 2023). Similarly, in earth sciences and healthcare, FM and diffusion models are deployed for global weather forecasting (Chen & Lipman, 2024; Price et al., 2025; Andrae et al., 2025; Chan et al., 2024), clinical time-series modeling (Zhang et al., 2024), as well as, general time-series forecasting (Kolloviev et al., 2024; 2023). However, while these works demonstrate the efficacy of generative models for high-fidelity regression, they typically prioritize in-distribution performance. They lack intrinsic mechanisms to flag off-manifold queries, relying entirely on the model’s ability to extrapolate, which poses severe risks in safety-critical deployments.

2.2. Off-Manifold Detection with Generative Models

While extensive literature exists for OOD detection in discriminative models (Liang et al., 2017; Sun et al., 2022; Li et al., 2023), addressing this challenge in conditional generative models remains underexplored. Prior unsupervised efforts primarily rely on likelihood criteria or reconstruction scores. However, likelihood-based approaches are not sufficient (Nalisnick et al., 2018; Hendrycks et al., 2018). Attempts to mitigate this via input complexity corrections (Serrà et al., 2019) or generative ensembles (Choi et al., 2018) have met with limited success, often functioning as computationally expensive post-hoc solutions than tackling the root cause.

Similarly, reconstruction-based methods using autoencoders or diffusion models (Liu et al., 2023; Graham et al., 2023) detect anomalies based on restoration errors. While effective as solely OOD detector, these strategies operate on the *output* space, assessing generation quality rather than validating the conditioning input itself, and typically serve as expensive external wrappers rather than integrated safety mechanisms.

Lastly, DiffPath (Heng et al., 2024) proposes a passive detection strategy based on analyzing the dynamics of the reverse generation process. However, the applicability of this framework to our setting is restricted by two structural differences. First, it is designed strictly for unconditional

models and has not been extended to conditional generation. Consequently, it inherently lacks a mechanism to explicitly evaluate the validity of the conditioning input. Second, the method relies on the specific curvature of diffusion SDE trajectories. It is incompatible with OT-FM, where Optimal Transport induces straight-line geodesics that erase the geometric signals DiffPath requires.

3. Diverging Flows

3.1. Problem Formulation

We define the task of *Extrapolation-Aware Probabilistic Regression* as learning a mapping $f_\theta : \mathcal{X} \rightarrow \mathcal{P}(\mathcal{Y}) \times \mathbb{R}$ that outputs both a predictive distribution and an extrapolation indicator. Formally, for an input x :

$$f_\theta(x) = (p_\theta(y|x), S_\theta(x)) \quad (1)$$

where $p_\theta(\cdot|x)$ approximates the conditional data density $p_{data}(y|x)$, and $S_\theta(x)$ serves as an extrapolation score.

To ensure safety, this tuple must satisfy two critical properties: (i) *Fidelity*, where for in-distribution inputs ($x \in \mathcal{M}_{ID}$), p_θ minimizes the divergence from the true conditional distribution; and (ii) *Trust*, where the score acts as a discriminator for manifold membership, effectively separating valid from invalid inputs such that $S_\theta(\tilde{x}) > S_\theta(x)$ for any $\tilde{x} \notin \mathcal{M}_{ID}$ and $x \in \mathcal{M}_{ID}$.

3.2. Flow Matching

We realize the predictive component of our formulation using the OT-FM framework (Lipman et al., 2022). For consistency with FM literature, we denote the target state as $x \in \mathcal{X}$ and the conditioning input as $c \in \mathcal{C}$. While we frame our analysis in terms of probabilistic regression, this formulation is mathematically general and naturally extends to **conditional generation tasks**.

The generative process in conditional generation is governed by the flow ODE:

$$\frac{d\psi_t(x)}{dt} = v_t^\theta(\psi_t(x), c), \quad (2)$$

where $t \in [0, 1]$, and v_t^θ is a neural vector field that pushes a noise prior p_0 to the target density $p_1(\cdot|c)$. This probabilistic formulation naturally handles aleatoric uncertainty arising from inherent data noise. By sampling N trajectories $\{\psi_1^{(i)}(c)\}_{i=1}^N \sim p_\theta(\cdot|c)$ generated by solving Eq. 2, we approximate the conditional expectation to obtain a robust prediction:

$$\hat{x} = \mathbb{E}_{p_\theta}[x|c] \approx \frac{1}{N} \sum_{i=1}^N \psi_1(x_0^{(i)}; c). \quad (3)$$

While this Monte Carlo integration effectively filters stochastic noise, it fails to guarantee model trustworthiness. For an off-manifold condition \tilde{c} disjoint from the training support, the FM continues to generate a coherent, low-variance predictive distribution, yielding a plausible but extrapolated prediction \hat{x} , rendering the standard estimator insufficient for safety-critical applications.

3.3. The Extrapolation Risk

Let $\mathcal{X} = \mathbb{R}^d$ denote the data space and $\mathcal{C} = \mathbb{R}^k$ the conditioning space. We assume valid conditions lie on a lower-dimensional manifold $\mathcal{M}_{ID} \subset \mathcal{C}$ with support defined by the data distribution $p_1(c)$. The complement $\mathcal{C}_{OOD} = \mathbb{R}^k \setminus \mathcal{M}_{ID}$ represents the off-manifold regime.

Optimal Transport theory establishes that the most efficient probability path follows the Euclidean geodesic $u_t^{OT}(x|x_1) = x_1 - x_0$, minimizing the kinetic energy of the transport (Benamou & Brenier, 2000). We define the *Transport Energy Excess*, $\mathcal{E}(v^\theta; c)$, as the deviation of the learned vector field from this optimal geodesic:

$$\mathcal{E}(v^\theta; c) = \mathbb{E}_{t,x_t} [\|v_t^\theta(x_t, c) - u_t^{OT}(x_t|x_1)\|^2]. \quad (4)$$

We highlight that minimizing $\mathcal{E}(v^\theta; c)$ is equivalent to the OT-FM objective, L_{FM} (Lipman et al., 2022). Thus, standard training explicitly optimizes for efficiency, unintentionally enforcing the silent failure mode on invalid inputs.

Ideally, a safe predictor would exhibit a *geometric phase transition*: minimizing $\mathcal{E}(v^\theta; c) \rightarrow 0$ for $c \in \mathcal{M}_{ID}$ (high fidelity) while maximizing $\mathcal{E}(v^\theta; \tilde{c}) \gg 0$ for $\tilde{c} \in \mathcal{C}_{OOD}$ (detectable divergence).

However, for the ODE solution ψ_t to be unique and well-defined, the vector field u_t must be locally Lipschitz continuous with respect to c (Coddington & Levinson, 1955; Lipman et al., 2024). That is, there exists a constant K such that for any $x \in \mathcal{X}$ and $c, c' \in \mathcal{C}$:

$$\|u_t(x, c) - u_t(x, c')\|_2 \leq K\|c - c'\|_2. \quad (5)$$

Combined with the spectral bias of deep neural networks (Rahaman et al., 2019), which preferentially learns low-frequency functions, the trained model inherently minimizes this Lipschitz constant K . This regularity creates a fundamental *extrapolation hazard*. For any off-manifold query \tilde{c} residing in an ϵ -neighborhood of a valid condition $c \in \mathcal{M}_{ID}$, the change in transport energy is bounded by the Lipschitz property:

$$|\mathcal{E}(v^\theta; \tilde{c}) - \mathcal{E}(v^\theta; c)| \leq L \cdot \|\tilde{c} - c\|_2 \approx 0 \quad (6)$$

where L is a constant dependent on K . Since $\mathcal{E}(v^\theta; c) \approx 0$ for valid data (by training), the inequality forces $\mathcal{E}(v^\theta; \tilde{c}) \approx 0$. Eq. 6 constrains pointwise velocities but not the full

trajectories defining $\mathcal{E}(v^\theta; \tilde{c})$, yet it describes the silent extrapolation behavior observed in FM models. Consequently, the model predicts efficient paths even for invalid inputs. This silent failure creates trajectories that resemble valid ones, making standard detection ineffective. We attribute this to the smoothness of the vector field: without explicit penalties, the model defaults to the simplest path for any input, regardless of its validity.

3.4. Contrasting Vector Fields

To enforce the geometric property described in Sec. 3.3, we adapt contrastive learning principles (Hadsell et al., 2006; Chen et al., 2020). Traditionally, contrastive learning organizes data in an embedding space by pulling semantically similar inputs (positives) together while pushing dissimilar ones (negatives) apart. We extend this logic to the space of vector fields, treating the optimal geodesic u_t^{OT} as a *geometric anchor*. By pulling valid vector fields toward this anchor and pushing off-manifold ones away, we induce a controlled violation of the smoothness bias. This locally maximizes the Lipschitz constant at the manifold boundary, transforming the smooth extrapolation into a sharp gradient that signals invalidity.

Let (x_1, c) be a valid data-condition pair from the training set. We define the predicted velocity field under the valid condition, $\hat{u}_{t,c} = v_t^\theta(x_t, c)$, as the positive sample, and the velocity field under the off-manifold condition, $\hat{u}_{t,\tilde{c}} = v_t^\theta(x_t, \tilde{c})$, as the negative sample.

We introduce two margin-based penalty terms inspired by triplet loss objectives (Balntas et al., 2016). These terms constrain the geometric relationship between the target vector field u_t and the model’s predictions.

First, the repulsion loss (L_{repel}) encourages separation in Euclidean magnitude, ensuring that the error for the off-manifold condition is significantly higher than for the on-manifold condition. Second, the curvature loss (L_{curve}) promotes directional divergence, penalizing off-manifold flows that align with the optimal transport path. We define these formally as:

$$L_{\text{repel}} = \max\{d_1(u_t, \hat{u}_c) - d_1(u_t, \hat{u}_{\tilde{c}}) + m_r, 0\} \quad (7)$$

$$L_{\text{curve}} = \max\{d_2(u_t, \hat{u}_c) - d_2(u_t, \hat{u}_{\tilde{c}}) + m_c, 0\} \quad (8)$$

where $d_1(a, b) = \|a - b\|_2$ is the Euclidean distance, and $d_2(a, b) = 1 - \frac{a \cdot b}{\|a\| \|b\|}$ is the cosines distance. The hyperparameters m_r and m_c represent the desired margin of separation for magnitude and angle, respectively.

The final training objective, *Diverging Flows* (DiFlo), combines the FM loss with these contrastive regularizers:

$$L_{\text{DiFlo}} = \|u_t^{OT} - v_t^\theta(x_t, c)\|^2 + \lambda L_{\text{repel}} + \beta L_{\text{curve}} \quad (9)$$

where λ and β , the weights of each contrastive component.

This objective equips the model with an implicit ability to capture the manifold of valid conditions. The repulsion term forces the kinetic energy of off-manifold flows to deviate from the optimal transport cost, while the curvature term steers the vector field orthogonally to the geodesic path. As a result, solving the ODE (Eq. 2) yields flows that diverge substantially depending on the conditioning input, as illustrated in Figure 1.

3.5. Negative Sample Creation

The effectiveness of the contrastive objective is dependent on the quality of the negative samples. Random noise is often too easy to distinguish, failing to shape the decision boundary tightly around the \mathcal{M}_{ID} . To induce a sharp geometric transition, we require hard negatives, inputs that occupy the ϵ -neighborhood of the valid support but violate the underlying properties.

We employ an adversarial outlier mining strategy. We define the optimal negative sample \tilde{c}^* as the local perturbation that maximizes the model’s transport energy, effectively identifying the direction of highest geometric sensitivity:

$$\tilde{c}^* = \underset{\tilde{c}: \|\tilde{c} - c\| \leq \epsilon}{\text{argmax}} \|v_t^\theta(x_t, \tilde{c}) - u_t^{OT}\|^2. \quad (10)$$

In practice, we use Projected Gradient Descent (PGD) (Madry et al., 2017). PGD performs an iterative ascent along the gradient of L_{FM} , projecting perturbations back onto the ϵ -ball $\mathcal{B}_\epsilon(c)$ at each step:

$$\tilde{c}_{k+1} = \Pi_{\mathcal{B}_\epsilon(c)}(\tilde{c}_k + \eta \cdot \text{sgn}(\nabla_{\tilde{c}} \mathcal{L}_{FM}(\tilde{c}_k))). \quad (11)$$

We employ PGD to target local directions where the model attempts to generalize via smoothness, rather than enumerating infinite off-manifold inputs. Because the model relies on Lipschitz continuity to extend valid transport dynamics to off-manifold regions, structurally breaking this smoothness at the immediate boundary forces the model to implicitly learn the valid support. For the training algorithm of Diverging Flows see Appendix A.1.

3.6. Detection of Off-Manifold Inputs

We propose a detection metric grounded in the geometry of OT-FM. As established in the previous section, the target probability path for valid data is the straight line connecting the source p_0 and the target p_1 (Lipman et al., 2022).

At inference time, given a starting noise sample x_0 and a condition c , the model generates a trajectory $\{\hat{x}_t\}_{t=0}^1$ ending at the predicted sample \hat{x}_1 . Hence, we can evaluate the *efficiency* of the path taken to reach the prediction. We define the ideal optimal transport trajectory x_t^{opt} as the direct linear interpolation between the start and the generated end, $x_t^{\text{opt}} = (1 - t)x_0 + t\hat{x}_1$, where $t \in [0, 1]$.

A well-trained FM model conditioned on on-manifold data approximates this linear path, resulting in a generated trajectory where $\hat{x}_t \approx x_t^{\text{opt}}$. Conversely, our contrastive objective (Eq. 9) prompts the vector field to diverge significantly from this linearity when the condition is off-manifold.

To quantify this behavior, we introduce the *Divergence from Optimal Trajectory* (DOT) score. We define the DOT score as the integral of the L_1 distance between the generated trajectory \hat{x}_t and the ideal linear interpolant x_t^{opt} over the generation interval:

$$S_{\text{DOT}}(\hat{x}_{0:1}) = \int_0^1 \|\hat{x}_t - x_t^{\text{opt}}\|_1 dt. \quad (12)$$

This metric effectively measures the area between the actual flow path and the chord connecting x_0 and \hat{x}_1 . In practice, we solve the flow ODE using a numerical solver with N discrete time steps $\{t_0, \dots, t_N\}$. The discrete approximation of the S_{DOT} score, averaged over spatial dimensions D , is given by:

$$\hat{S}_{\text{DOT}} = \sum_{i=0}^N \left(\frac{1}{D} \sum_{d=1}^D |\hat{x}_{t_i}^{(d)} - x_{t_i}^{\text{opt}^{(d)}}| \right) \quad (13)$$

where $\hat{x}_{t_i}^{(d)}$ is the value of the d -th dimension of the generated trajectory at time step t_i , and $x_{t_i}^{\text{opt}^{(d)}}$ is the corresponding value on the ideal linear path. This metric captures the turbulence induced by our contrastive training. While on-manifold flows remain nearly straight (yielding $\hat{S}_{\text{DOT}} \approx 0$), extrapolation flows exhibit significant curvature and deviation from the geodesic (Figure 1), resulting in positive, large \hat{S}_{DOT} values. For the algorithmic formulation of the inference refer to Appendix A.2.

3.7. Split Conformal Prediction

To ensure safety-critical reliability, we employ split conformal prediction (Gammerman et al., 1998; Angelopoulos et al., 2024) to construct a statistically valid decision boundary. Given a user-specified error rate $\alpha \in (0, 1)$, our goal is to identify a validity interval $[q_{lo}, q_{hi}]$ such that the probability of a valid on-manifold input falling outside this range is bounded by α .

We reserve a calibration dataset of M exchangeable on-manifold conditions. We first compute the \hat{S}_{DOT} for these samples and sort them in ascending order, denoting the sorted scores as $\mathcal{S}_{\text{cal}} = \{s_{(1)}, s_{(2)}, \dots, s_{(M)}\}$. We implement a two-sided conformal interval approach to determine the decision boundaries. Specifically, we distribute the error budget α equally between the lower and upper tails of the distribution. We calculate the indices for the lower and upper bounds as $k_{lo} = \lfloor (M+1) \frac{\alpha}{2} \rfloor$ and $k_{hi} = \lceil (M+1)(1 - \frac{\alpha}{2}) \rceil$. The decision thresholds are then defined by the scores at these ranks: $q_{lo} = s_{(k_{lo})}$ and $q_{hi} = s_{(k_{hi})}$.

At inference time, a query condition c_{test} is accepted as in-distribution if and only if its score lies within the calibrated interval: $q_{lo} \leq \hat{S}_{\text{DOT}}(x(c_{\text{test}})) \leq q_{hi}$

If the score falls outside this range, the input is flagged as invalid. Based on the exchangeability of the calibration and test data, this procedure provides a rigorous guarantee on the marginal coverage. The probability that a valid on-manifold input is correctly accepted satisfies, $\mathbb{P}(q_{lo} \leq \hat{S}_{\text{DOT}}(x_{\text{test}}) \leq q_{hi}) \geq 1 - \alpha$. This ensures that the False Positive Rate (FPR), the rate at which valid inputs are incorrectly rejected, is controlled at level α .

4. Experiments

We evaluate Diverging Flows (DiFlo) across three distinct regimes that showcase the geometric behavior and deployment viability: (i) geometric verification on synthetic manifolds, (ii) weather temperature forecasting, and (iii) cross-domain style transfer. Since no existing Flow or Diffusion models inherently integrate off-manifold detection, we benchmark primarily against standard FM. To strictly evaluate intrinsic extrapolation detection, we exclude methods requiring auxiliary networks or post-hoc pipelines, instead evaluating the baseline via two distinct scoring mechanisms. First, we employ our proposed DOT score on the standard model; this acts a verification that detection capabilities stem from the contrastive reshaping of the vector field rather than the metric alone. Second, we compare against the FM model's likelihood, representing the conventional statistical approach. Following Lipman et al. (2024), we estimate this using the instantaneous change of variables formula with Hutchinson's trace estimator:

$$\log p_1(\psi_1(x)) = \log p_0(\psi_0(x)) - \mathbb{E}_Z \int_0^1 \text{tr}[Z^T \partial_x v_t(\psi_t(x)) Z] dt, \quad (14)$$

where $Z \in \mathbb{R}^{d \times d}$ is a random variable with $\mathbb{E}[Z] = 0$ and $\text{Cov}(Z, Z) = I$. This formulation allows for scalable likelihood estimation via vector-Jacobian products. Finally, for completeness, we provide a pure detection benchmark comparing Diverging Flows against the DiffPath detector in Appendix B.4.

We quantify *Safety* via two metrics: (1) the AUROC (Fawcett, 2006), measuring global separability; and (2) the FPR governed by split conformal prediction constraints. We calibrate a decision region \mathcal{C}_α to guarantee a marginal coverage of $1 - \alpha$ for on-manifold inputs. The FPR reports the percentage of off-manifold anomalies \tilde{c} that incorrectly satisfy this condition, defined formally as $\text{FPR} = \mathbb{P}(S(\tilde{c}) \in \mathcal{C}_\alpha \mid \tilde{c} \notin \mathcal{M}_{ID})$. For *Fidelity*, we ensure our contrastive objective does not degrade predictive performance using task-specific metrics. In regression, we monitor physical consistency via Mean Squared Error (MSE = $\mathbb{E}[\|y - \hat{y}\|_2^2]$),

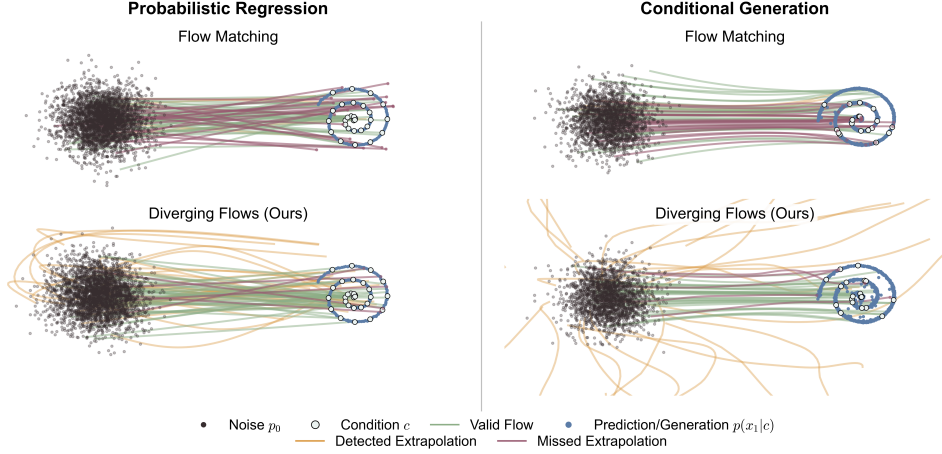


Figure 2. Vector Dynamics on Synthetic Manifolds. Two experiments, Probabilistic Regression (left), with horizon of 10 steps, and Conditional Generation (right). Top: Standard FM forces smooth convergence for all inputs, causing silent hallucinations. Bottom: Diverging Flows learns a conservative field: on-manifold inputs (green) follow optimal paths, while off-manifold queries (orange) trigger divergent flows, creating a geometric detection signal.

Peak Signal-to-Noise Ratio (PSNR) (Hore & Ziou, 2010), and Structural Similarity (SSIM) (Wang et al., 2003; 2004). In generative tasks, we assess distribution quality via the Fréchet Inception Distance (Heusel et al., 2017), defined as $\text{FID} = \|\mu_r - \mu_g\|^2 + \text{Tr}(\Sigma_r + \Sigma_g - 2(\Sigma_r \Sigma_g)^{1/2})$, and Perceptual Similarity (LPIPS) (Zhang et al., 2018). Detailed hyperparameters and architecture specifications are provided in Appendix B.

4.1. Synthetic Manifold Experiments

We validate our framework on a 2D spiral manifold $\mathcal{M}_{ID} \subset [-1, 1]^2$ parameterized by $\theta \sim \mathcal{U}[0, 5\pi]$. A valid sample $x(\theta)$ is defined as: $x(\theta) = r(\theta)(\cos \theta \ \sin \theta)^\top + \xi$, where $\xi \sim \mathcal{N}(0, \sigma^2 I)$, $r(\theta) = \frac{\theta}{5\pi}$ is the normalized radius and $\sigma = 0.005$ represents intrinsic noise. The out-of-distribution set is defined as the ambient space strictly separated from the manifold support: $\mathcal{C}_{OOD} = \{c \in [-1, 1]^2 \mid \min_{c' \in \mathcal{M}_{ID}} \|c - c'\|_2 > \epsilon\}$.

We evaluate two conditional tasks: (i) **Probabilistic Regression**: Given a current state $c = x(\theta_k)$, the model predicts the future trajectory $y = [x(\theta_{k+1}), \dots, x(\theta_{k+10})]$. This tests the preservation of local dynamics alongside the ability to reject invalid inputs. (ii) **Conditional Generation**: The model learns $p_\theta(x|c) \approx p_1(x)$ for any valid condition $c \in \mathcal{M}_{ID}$, subject to $x \neq c$. Here, c acts as a validity token; off-manifold conditions must trigger vector field divergence rather than sampling valid data. The results of the experiments are illustrated in Figure 2, where we show how the flow ODE of FM and DiFlo behaves when an off-manifold input is encountered.

Ablation Study. To isolate the contribution of each objective component, we compare Diverging Flows against

three variants: (i) w/o \mathcal{L}_{repel} ($\lambda = 0$) to test directional divergence alone; (ii) w/o \mathcal{L}_{curve} ($\beta = 0$) to test magnitude penalties alone; and (iii) Random Noise, replacing PGD negative mining with $\tilde{c} \sim \mathcal{U}[-1, 1]$ to validate the necessity of adversarial examples.

Table 1. Results on Synthetic Manifolds. We report detection metrics (AUROC, FPR) for both tasks and predictive accuracy (MSE) for regression. FM fails to detect off-manifold inputs effectively, while Diverging Flows achieves consistently high separation (> 0.98 AUROC) with low FPR after the conformal calibration.

Algorithm	AUROC \uparrow	FPR(%) \downarrow	MSE \downarrow
Conditional Generation			
FM-Likelihood	0.510	94.62	—
FM-DOT	0.507	95.10	—
DiFlo (Ours)	0.981	5.46	—
Probabilistic Regression			
FM-Likelihood	0.565	93.32	6×10^{-4}
FM-DOT	0.602	92.34	6×10^{-4}
DiFlo w/o \mathcal{L}_{repel}	0.711	10.45	7×10^{-4}
DiFlo w/o \mathcal{L}_{curve}	0.931	20.69	5 $\times 10^{-4}$
DiFlo w/ $\tilde{c} \sim \mathcal{U}[-1, 1]$	0.662	90.45	7×10^{-4}
DiFlo (Ours)	0.998	3.45	7×10^{-4}

In Table 1, we empirically confirm the smoothness hazard inherent to Flow Matching. The baseline yields AUROC scores near 0.50 for both tasks, effectively reducing off-manifold detection to random guessing. This proves that without explicit constraints, the model extrapolates efficient linear paths even for invalid inputs. In contrast, Diverging Flows induces a sharp geometric transition, achieving consistently high separation (AUROC > 0.98) while maintaining predictive fidelity comparable to the baseline. This confirms that safety can be embedded into the vector field

without compromising in-distribution dynamics.

The ablation study highlights the critical role of PGD. Replacing PGD with random noise negatives degrades performance significantly (AUROC 0.662), confirming that easy negatives fail to tighten the vector field around the manifold support. Furthermore, we observe that the repulsion term \mathcal{L}_{repel} is the primary driver of the detection signal; removing it causes a sharper drop in performance compared to removing the curvature penalty \mathcal{L}_{curve} , though both are required for optimal separation.

4.2. Weather Temperature Forecasting

We evaluate the deployment viability of Diverging Flows on the ERA5 dataset (Hersbach et al., 2020), by forecasting surface temperature heatmaps (64×64) six hours into the future. The model $p_\theta(x_{t+6h}|x_t)$ is parameterized as a U-Net, where the current atmospheric state x_t is injected via cross-attention layers to condition the generation of the future state.

This domain demands strict adherence to physical laws; a reliable model must reject inputs that violate thermodynamic principles. To test the physical consistency, we adopt the artificial hotspot setup from Chan et al. (2024). We perturb valid inputs by injecting thermal anomalies into historically cold regions. These perturbations are semantically plausible as images but violate local thermodynamic laws. A conservative forecaster must identify these inputs as physically infeasible rather than hallucinating. We compare our method against standard FM and HyperDM, the diffusion-based baseline proposed in the original benchmark, however, this approach does not provide off-manifold detection.

Table 2. Weather Temperature Forecasting Performance (ERA5). We compare predictive fidelity (MSE, SSIM, PSNR) and detection (AUROC). Diverging Flows achieves robust detection of physical anomalies (0.98 AUROC), while maintaining competitive predictive fidelity on valid forecasts, compared to the random guessing of the FM baseline.

Algorithm	MSE ↓	SSIM ↑	PSNR ↑	AUROC ↑
HyperDM	0.004	0.954	33.15	—
FM-Likelihood	0.0038	0.955	34.23	0.556
FM-DOT	0.0038	0.955	34.23	0.601
DiFlo (Ours)	0.0034	0.951	34.03	0.980

Table 2 demonstrate that standard models fail to capture physical constraints. The FM baseline yields a near-random AUROC because it ignores the violation, treating the hotspot as valid high-frequency noise, as illustrated in Figure 3. Compared to the HyperDM baseline, flow-based methods perform slightly better, in terms of predictive fidelity.

In contrast, Diverging Flows achieves near-perfect detection. By altering the transport for invalid inputs, the model

effectively learns to check for physical validity. Critically, this mechanism improves predictive fidelity, since Diverging Flows achieves an MSE of 0.0034, while slightly decreasing in SSIM metric. This confirms that geometric regularization effectively filters unphysical dynamics without hindering the learning of valid temperature patterns. Lastly, conformal prediction ($\alpha = 0.05$) yields a 5.20% FPR, providing a rigorous statistical guarantee of 95% coverage while identifying extrapolations.

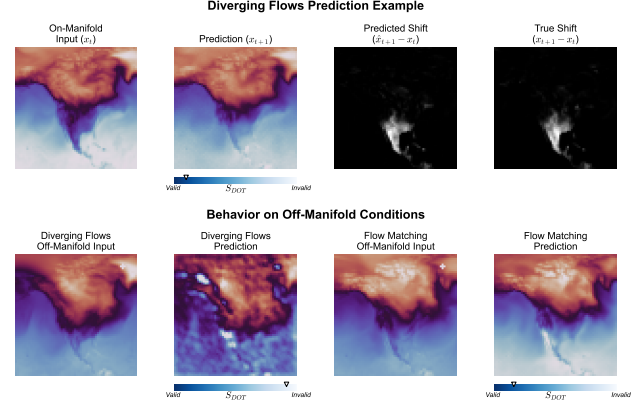


Figure 3. High-Fidelity Forecasts with Diverging Flows. (Top) Visual comparison of 6-hour temperature forecasts. Diverging Flows accurately captures complex thermal fronts and fine-grained dynamics with MSE and SSIM of 0.0004 and 0.961 respectively, demonstrating that the regularization for hallucination detection does not compromise the model’s capacity for precise physical regression. (Bottom) Comparison of the behavior of Diverging Flows and FM when an invalid condition is encountered.

4.3. Cross-Domain Style Transfer

Finally, we investigate the model’s ability to handle structurally disjoint conditioning manifolds by mapping grayscale MNIST digits (c) (LeCun & Cortes, 1998) to RGB Street House View Numbers (SVHN) (x) (Netzer et al., 2011). We introduce Fashion-MNIST (FMNIST) (Xiao et al., 2017) and Kuzushiji-MNIST (KMNIST) (Clanuwat et al., 2018) to probe whether Diverging Flows implicitly captures the semantic support of valid conditions. FMNIST represents a clear *structural shift* (clothing vs. digits), whereas KMNIST poses a harder *semantic shift*, sharing significant low-level statistics (e.g., stroke density) with MNIST.

Table 3 highlights that FM ignores the semantic meaning, since it extrapolates confident paths for KMNIST (near-random AUROC). In contrast, Diverging Flows imposes a robust boundary via PGD, learning to reject non-digit concepts (> 0.86 AUROC). Crucially, this awareness comes with negligible cost to generation quality; as shown in Figure 4, the model retains expressivity for valid inputs, confirming that geometric regularization targets invalid semantics without constraining the valid generative distribution.

Table 3. Cross-Domain Style Transfer Results. We evaluate generation quality (FID, LPIPS) and detection (AUROC) against structural (FMNIST) and semantic (KMNIST) shifts. Diverging Flows successfully learns a semantic boundary, rejecting invalid queries without degrading the generative quality (FID) compared to the baseline.

Algorithm	FID-50K ↓ LPIPS ↓		AUROC ↑	
	vs FMNIST vs KMNIST			
FM-Likelihood	4.102	0.2172	0.529	0.516
FM-DOT	4.102	0.2172	0.527	0.513
DiFlo (Ours)	4.104	0.2202	0.955	0.860

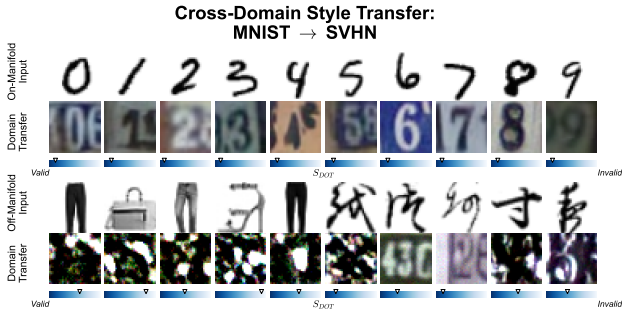


Figure 4. Generative Quality in Cross-Domain Transfer. Samples mapping structural inputs (MNIST) to street-view imagery (SVHN). Diverging Flows preserves the semantic identity of the digit. This demonstrates that regularization targets invalid semantics without restricting diversity.

4.4. Efficacy of Negative Sampling Strategies

To isolate the contribution of our adversarial negative mining, we compare Diverging Flows trained with PGD against three alternative negative sampling strategies: (i) **Heuristics**: Domain-specific augmentations (random resized crops, rotations, and Gaussian blur) intended to create near-manifold perturbations; (ii) **Masking**: Random and checkerboard masking strategies that remove spatial information; and (iii) **Outlier Exposure**: Using the Omniglot (Lake et al., 2015) dataset as a source of explicit, fixed negative samples.

Table 4. Negative Sampling Ablation. Comparison of sampling strategies across domains. While domain-specific heuristics fail to generalize (e.g., Weather), PGD achieves consistent high performance on all tasks.

Sampling Method	Temperature Forecasting		Style Transfer	
	Hotspots		FMNIST	KMNIST
Masking	0.729		0.654	0.541
Outlier Exposure	N/A		0.710	0.572
Domain Transforms	0.733		0.987	0.892
PGD (Ours)	0.980		0.955	0.860

The results in Table 4 highlight a limitation of static negative sampling: it requires prior knowledge of the manifold boundary. **Heuristic Transforms** perform exceptionally well on the digit tasks (outperforming PGD slightly on FM-

NIST/KMNIST) because shifts like rotation and cropping directly align with the known invariances of character recognition. However, the same strategy fails completely on the Weather task. In a physical system, a rotated pressure field is not an off-manifold sample, it is often a impossible or represents a completely different valid state, making simple augmentations insufficient for defining the boundary of thermodynamic validity, without the required domain knowledge. Similarly, **Outlier Exposure** and **Masking** struggle to generalize. Outlier exposure effectively overfits to the specific negative dataset (Omniglot) and fails to detect shifts in semantic structure (FMNIST) that do not resemble the training negatives.

In contrast, **PGD** proves to be the only modality-agnostic solution. By dynamically optimizing for the hardest negative in the local neighborhood of the input, PGD automatically discovers the relevant boundary constraints. While it may be slightly outperformed by hand-crafted heuristics in simple domains, it achieves consistent, high-performance detection across domains without requiring manual, domain-specific engineering.

5. Conclusion and Limitations

Diverging Flows allows a single Flow Matching model to simultaneously perform high-fidelity prediction and intrinsic extrapolation detection. Our core contribution is the formulation of a geometric phase transition: by actively enforcing trajectory divergence for off-manifold inputs, we transform the vector field from a generator into a self-monitoring mechanism. This shifts extrapolation detection from a post-hoc statistical estimation problem to a geometric constraint, ensuring that safety is an inherent property of the dynamics rather than an external add-on. Crucially, this design of Diverging Flows introduces zero inference overhead, establishing it as a robust solution for real-time critical applications.

A limitation of our approach is the training overhead required to create hard negatives via iterative adversarial updates. Additionally, our current formulation relies on Euclidean Optimal Transport; but the contrastive principles developed here can easily be extended to Riemannian manifolds, which would make it effective to support geometric deep learning tasks (Chen & Lipman, 2024). Finally, we plan to deploy Diverging Flows in real-world robotic tasks, where detecting extrapolations is essential to avert potentially harmful outcomes.

Acknowledgments

This work was supported by a DGA-Inria contract (ATOR Project), the EU Horizon project euROBIN (GA n.101070596), and the France 2030 program through the PEPR O2R projects AS3 and PI3 (ANR-22-EXOD-007,

ANR-22-EXOD).

Impact Statement

The goal of this work is to advance the reliability of generative models in scientific and industrial tasks. By enabling models to detect and reject extrapolations, our method mitigates the risks of silent hallucinations in safety-critical applications such as weather forecasting, autonomous systems, and scientific discovery. We believe this work contributes positively to the responsible deployment of machine learning in high-stakes domains by transforming invisible failure modes into detectable signals. We do not foresee specific negative societal consequences, as the primary focus of this work is to advance machine learning for reliability and transparency.

References

Andrae, M., Landelius, T., Oskarsson, J., and Lindsten, F. Continuous ensemble weather forecasting with diffusion models. In *The Thirteenth International Conference on Learning Representations*, 2025.

Angelopoulos, A. N., Barber, R. F., and Bates, S. Theoretical foundations of conformal prediction. *arXiv preprint arXiv:2411.11824*, 2024.

Balntas, V., Riba, E., Ponsa, D., and Mikolajczyk, K. Learning local feature descriptors with triplets and shallow convolutional neural networks. In *Bmvc*, volume 1, pp. 3, 2016.

Benamou, J.-D. and Brenier, Y. A computational fluid mechanics solution to the monge-kantorovich mass transfer problem. *Numerische Mathematik*, 84(3):375–393, 2000.

Black, K., Brown, N., Driess, D., Esmail, A., Equi, M., Finn, C., Fusai, N., Groom, L., Hausman, K., Ichter, B., et al. π_0 : A vision-language-action flow model for general robot control. *arXiv preprint arXiv:2410.24164*, 2024.

Bose, A. J., Akhound-Sadegh, T., Huguet, G., Fatras, K., Rector-Brooks, J., Liu, C.-H., Nica, A. C., Korablyov, M., Bronstein, M., and Tong, A. Se (3)-stochastic flow matching for protein backbone generation. *arXiv preprint arXiv:2310.02391*, 2023.

Cao, X. and Yousefzadeh, R. Extrapolation and ai transparency: Why machine learning models should reveal when they make decisions beyond their training. *Big Data & Society*, 10(1):20539517231169731, 2023. doi: 10.1177/20539517231169731.

Chalapathy, R. and Chawla, S. Deep learning for anomaly detection: A survey. *arXiv preprint arXiv:1901.03407*, 2019.

Chan, M., Molina, M., and Metzler, C. Estimating epistemic and aleatoric uncertainty with a single model. *Advances in Neural Information Processing Systems*, 37:109845–109870, 2024.

Chen, R. T., Rubanova, Y., Bettencourt, J., and Duvenaud, D. K. Neural ordinary differential equations. *Advances in Neural Information Processing Systems*, 31, 2018.

Chen, R. T. Q. and Lipman, Y. Flow matching on general geometries. In *The Twelfth International Conference on Learning Representations*, 2024.

Chen, T., Kornblith, S., Norouzi, M., and Hinton, G. A simple framework for contrastive learning of visual representations. In *International Conference on Machine Learning*, pp. 1597–1607. PMLR, 2020.

Chi, C., Xu, Z., Feng, S., Cousineau, E., Du, Y., Burchfiel, B., Tedrake, R., and Song, S. Diffusion policy: Visuomotor policy learning via action diffusion. *The International Journal of Robotics Research*, pp. 02783649241273668, 2023.

Choi, H., Jang, E., and Alemi, A. A. Waic, but why? generative ensembles for robust anomaly detection. *arXiv preprint arXiv:1810.01392*, 2018.

Clanuwat, T., Bober-Irizar, M., Kitamoto, A., Lamb, A., Yamamoto, K., and Ha, D. Deep learning for classical japanese literature. *arXiv preprint arXiv:1812.01718*, 2018.

Coddington, E. A. and Levinson, N. Theory of ordinary differential equations. 1955.

Cui, Y., Liu, Z., and Lian, S. A survey on unsupervised anomaly detection algorithms for industrial images. *IEEE Access*, 11:55297–55315, 2023. doi: 10.1109/ACCESS.2023.3282993.

Fawcett, T. An introduction to roc analysis. *Pattern recognition letters*, 27(8):861–874, 2006.

Gammerman, A., Vovk, V., and Vapnik, V. Learning by transduction. In *Proceedings of the Fourteenth Conference on Uncertainty in Artificial Intelligence*, UAI’98, pp. 148–155, San Francisco, CA, USA, 1998. Morgan Kaufmann Publishers Inc. ISBN 155860555X.

Graham, M. S., Pinaya, W. H., Tudosiu, P.-D., Nachev, P., Ourselin, S., and Cardoso, J. Denoising diffusion models for out-of-distribution detection. In *Proceedings of the IEEE/CVF Conference on Computer Vision and Pattern Recognition*, pp. 2948–2957, 2023.

Guerrero, J. J. A., Inoue, N., Masui, K., Otani, M., and Nakayama, H. Layoutflow: flow matching for layout generation. In *European Conference on Computer Vision*, pp. 56–72. Springer, 2024.

Hadsell, R., Chopra, S., and LeCun, Y. Dimensionality reduction by learning an invariant mapping. In *2006 IEEE Computer Society Conference on Computer Vision and Pattern Recognition (CVPR'06)*, volume 2, pp. 1735–1742. IEEE, 2006.

Hendrycks, D., Mazeika, M., and Dietterich, T. Deep anomaly detection with outlier exposure. *arXiv preprint arXiv:1812.04606*, 2018.

Heng, A., Soh, H., et al. Out-of-distribution detection with a single unconditional diffusion model. *Advances in Neural Information Processing Systems*, 37:43952–43974, 2024.

Herrera-Poyatos, A., Del Ser, J., de Prado, M. L., Wang, F.-Y., Herrera-Viedma, E., and Herrera, F. Responsible artificial intelligence systems: A roadmap to society’s trust through trustworthy ai, auditability, accountability, and governance. *arXiv preprint arXiv:2503.04739*, 2025.

Hersbach, H., Bell, B., Berrisford, P., Hirahara, S., Horányi, A., Muñoz-Sabater, J., Nicolas, J., Peubey, C., Radu, R., Schepers, D., Simmons, A., Soci, C., Abdalla, S., Abellán, X., Balsamo, G., Bechtold, P., Biavati, G., Bidlot, J., Bonavita, M., De Chiara, G., Dahlgren, P., Dee, D., Diamantakis, M., Dragani, R., Flemming, J., Forbes, R., Fuentes, M., Geer, A., Haimberger, L., Healy, S., Hogan, R. J., Hólm, E., Janisková, M., Keeley, S., Laloyaux, P., Lopez, P., Lupu, C., Radnoti, G., de Rosnay, P., Rozum, I., Vamborg, F., Villaume, S., and Thépaut, J.-N. The era5 global reanalysis. *Quarterly Journal of the Royal Meteorological Society*, 146(730):1999–2049, 2020. doi: <https://doi.org/10.1002/qj.3803>.

Heusel, M., Ramsauer, H., Unterthiner, T., Nessler, B., and Hochreiter, S. Gans trained by a two time-scale update rule converge to a local nash equilibrium. *Advances in Neural Information Processing Systems*, 30, 2017.

Ho, J., Jain, A., and Abbeel, P. Denoising diffusion probabilistic models. *Advances in Neural Information Processing Systems*, 33:6840–6851, 2020.

Hore, A. and Ziou, D. Image quality metrics: Psnr vs. ssim. In *2010 20th International Conference on Pattern Recognition*, pp. 2366–2369. IEEE, 2010.

Jing, B., Berger, B., and Jaakkola, T. Alphafold meets flow matching for generating protein ensembles. In *NeurIPS 2023 Generative AI and Biology (GenBio) Workshop*, 2023.

Ki, T., Min, D., and Chae, G. Float: Generative motion latent flow matching for audio-driven talking portrait. In *Proceedings of the IEEE/CVF International Conference on Computer Vision*, pp. 14699–14710, 2025.

Kim, B., Kim, J., Kim, J., and Ye, J. C. Generalized consistency trajectory models for image manipulation. *arXiv preprint arXiv:2403.12510*, 2024.

Kolloviev, M., Ansari, A. F., Bohlke-Schneider, M., Zschiegner, J., Wang, H., and Wang, Y. B. Predict, refine, synthesize: Self-guiding diffusion models for probabilistic time series forecasting. *Advances in Neural Information Processing Systems*, 36:28341–28364, 2023.

Kolloviev, M., Lienen, M., Lüdke, D., Schwinn, L., and Günemann, S. Flow matching with gaussian process priors for probabilistic time series forecasting. *arXiv preprint arXiv:2410.03024*, 2024.

Lake, B. M., Salakhutdinov, R., and Tenenbaum, J. B. Human-level concept learning through probabilistic program induction. *Science*, 350(6266):1332–1338, 2015.

LeCun, Y. and Cortes, C. The mnist database of handwritten digits. 1998.

Li, J., Chen, P., He, Z., Yu, S., Liu, S., and Jia, J. Rethinking out-of-distribution (ood) detection: Masked image modeling is all you need. In *Proceedings of the IEEE/CVF Conference on Computer Vision and Pattern Recognition (CVPR)*, pp. 11578–11589, June 2023.

Liang, S., Li, Y., and Srikant, R. Enhancing the reliability of out-of-distribution image detection in neural networks. *arXiv preprint arXiv:1706.02690*, 2017.

Lipman, Y., Chen, R. T., Ben-Hamu, H., Nickel, M., and Le, M. Flow matching for generative modeling. *arXiv preprint arXiv:2210.02747*, 2022.

Lipman, Y., Havasi, M., Holderrieth, P., Shaul, N., Le, M., Karrer, B., Chen, R. T., Lopez-Paz, D., Ben-Hamu, H., and Gat, I. Flow matching guide and code. *arXiv preprint arXiv:2412.06264*, 2024.

Liu, Z., Zhou, J. P., Wang, Y., and Weinberger, K. Q. Unsupervised out-of-distribution detection with diffusion inpainting. In *International Conference on Machine Learning*, pp. 22528–22538. PMLR, 2023.

Lubold, S. and Taylor, C. N. Formal definitions of conservative probability distribution functions (pdfs). *Information Fusion*, 88:175–183, 2022.

Ma, Y., Jayaraman, D., and Bastani, O. Conservative offline distributional reinforcement learning. *Advances in Neural Information Processing Systems*, 34:19235–19247, 2021.

Madry, A., Makelov, A., Schmidt, L., Tsipras, D., and Vladu, A. Towards deep learning models resistant to adversarial attacks. *arXiv preprint arXiv:1706.06083*, 2017.

Mariani, G., Tallini, I., Postolache, E., Mancusi, M., Cosmo, L., and Rodolà, E. Multi-source diffusion models for simultaneous music generation and separation. In *The Twelfth International Conference on Learning Representations*, 2024.

Nalisnick, E., Matsukawa, A., Teh, Y. W., Gorur, D., and Lakshminarayanan, B. Do deep generative models know what they don't know? *arXiv preprint arXiv:1810.09136*, 2018.

Netzer, Y., Wang, T., Coates, A., Bissacco, A., Wu, B., Ng, A. Y., et al. Reading digits in natural images with unsupervised feature learning. In *NIPS Workshop on Deep Learning and Unsupervised Feature Learning*, volume 2011, pp. 7. Granada, 2011.

Price, I., Sanchez-Gonzalez, A., Alet, F., Andersson, T. R., El-Kadi, A., Masters, D., Ewalds, T., Stott, J., Mohamed, S., Battaglia, P., et al. Probabilistic weather forecasting with machine learning. *Nature*, 637(8044):84–90, 2025.

Rahaman, N., Baratin, A., Arpit, D., Draxler, F., Lin, M., Hamprecht, F., Bengio, Y., and Courville, A. On the spectral bias of neural networks. In *International Conference on Machine Learning*, pp. 5301–5310. PMLR, 2019.

Roussel, Q., Ferrari, A., Ivaldi, S., and Mouret, J.-B. Flow matching imitation learning for multi-support manipulation. In *2024 IEEE-RAS 23rd International Conference on Humanoid Robots (Humanoids)*, pp. 528–535. IEEE, 2024.

Roussel, Q., Donoso, C., Chen, F., Ivaldi, S., and Mouret, J.-B. Extremum flow matching for offline goal conditioned reinforcement learning. *arXiv preprint arXiv:2505.19717*, 2025.

Serrà, J., Álvarez, D., Gómez, V., Slizovskaia, O., Núñez, J. F., and Luque, J. Input complexity and out-of-distribution detection with likelihood-based generative models. *arXiv preprint arXiv:1909.11480*, 2019.

Shao, Z., Zhuang, L., Yan, J., and Chen, L. Conservative in-distribution q-learning for offline reinforcement learning. In *2024 International Joint Conference on Neural Networks (IJCNN)*, pp. 1–8, 2024. doi: 10.1109/IJCNN60899.2024.10650768.

Sohl-Dickstein, J., Weiss, E., Maheswaranathan, N., and Ganguli, S. Deep unsupervised learning using nonequilibrium thermodynamics. In *International Conference on Machine Learning*, pp. 2256–2265. PMLR, 2015.

Sun, Y., Ming, Y., Zhu, X., and Li, Y. Out-of-distribution detection with deep nearest neighbors. In *International Conference on Machine Learning*, pp. 20827–20840. PMLR, 2022.

Tong, A., Malkin, N., Huguet, G., Zhang, Y., Rector-Brooks, J., FATRAS, K., Wolf, G., and Bengio, Y. Improving and generalizing flow-based generative models with mini-batch optimal transport. In *ICML Workshop on New Frontiers in Learning, Control, and Dynamical Systems*, 2023.

Wang, Z., Simoncelli, E. P., and Bovik, A. C. Multiscale structural similarity for image quality assessment. In *The thirty-seventh asilomar conference on signals, systems & computers*, 2003, volume 2, pp. 1398–1402. IEEE, 2003.

Wang, Z., Bovik, A. C., Sheikh, H. R., and Simoncelli, E. P. Image quality assessment: from error visibility to structural similarity. *IEEE Transactions on Image Processing*, 13(4):600–612, 2004.

Xiao, H., Rasul, K., and Vollgraf, R. Fashion-mnist: a novel image dataset for benchmarking machine learning algorithms. *arXiv preprint arXiv:1708.07747*, 2017.

Zhang, R., Isola, P., Efros, A. A., Shechtman, E., and Wang, O. The unreasonable effectiveness of deep features as a perceptual metric. In *Proceedings of the IEEE Conference on Computer Vision and Pattern Recognition*, pp. 586–595, 2018.

Zhang, X. N., Pu, Y., Kawamura, Y., Loza, A., Bengio, Y., Shung, D., and Tong, A. Trajectory flow matching with applications to clinical time series modelling. *Advances in Neural Information Processing Systems*, 37:107198–107224, 2024.

A. Diverging Flows Algorithms

A.1. Training Algorithm

Below, we summarize the training algorithm of Diverging Flows.

Algorithm 1 Training of Diverging Flows

```

1: Input: Dataset  $\mathcal{D}$ , Parameters  $\lambda, \beta, \eta, K$ 
2: Initialize: Neural Network  $v_t^\theta$ 
3: for each iteration do
4:   1. Data Sampling
5:     Sample  $(x_1, c) \sim \mathcal{D}$ ,  $x_0 \sim p_0$ ,  $t \sim \mathcal{U}[0, 1]$ 
6:     Interpolate:  $x_t = (1 - t)x_0 + tx_1$ 
7:     Target velocity:  $v_t = x_1 - x_0$ 
8:   2. Standard Flow Matching
9:     Predict velocity:  $\hat{v}_c = v_t^\theta(x_t, c)$ 
10:     $\mathcal{L}_{FM} = \mathbb{E}_{t, x_0, x_1, c} [\|\hat{v}_c - v_t\|^2]$ 
11:   3. Adversarial Negative Mining (PGD)
12:     Initialize  $\tilde{c}_0 = c$ 
13:     for  $k = 1$  to  $K$  do
14:        $g = \nabla_{\tilde{c}} \|\hat{v}_{\tilde{c}_{k-1}} - v_t\|^2$ 
15:        $\tilde{c}_k = \tilde{c}_{k-1} + \eta \cdot \text{sign}(g)$ 
16:        $\tilde{c}_k = \text{Project}(\tilde{c}_k, \mathcal{B}_\epsilon(c))$ 
17:     end for
18:     Set final off-manifold condition:  $\tilde{c} = \tilde{c}_K$ 
19:   4. Contrastive Regularization
20:     Predict off-manifold velocity:  $\hat{v}_{\tilde{c}} = v_t^\theta(x_t, \tilde{c})$ 
21:     // Repulsion ( $L_2$ )
22:      $\mathcal{L}_{repel} = \mathbb{E}_{t, x_0, x_1, c} [\max(\|v_t - \hat{v}_c\|_2 - \|v_t - \hat{v}_{\tilde{c}}\|_2 + m_r, 0)]$ 
23:     // Curve
24:      $d_{cos}(a, b) = 1 - \frac{a \cdot b}{\|a\| \|b\|}$ 
25:      $\mathcal{L}_{curve} = \mathbb{E}_{t, x_0, x_1, c} [\max(d_{cos}(v_t, \hat{v}_c) - d_{cos}(v_t, \hat{v}_{\tilde{c}}) + m_c, 0)]$ 
26:   5. Optimization
27:     Total Loss:  $\mathcal{L} = \mathcal{L}_{FM} + \lambda \mathcal{L}_{repel} + \beta \mathcal{L}_{curve}$ 
28:     Update  $\theta$  using  $\nabla_\theta \mathcal{L}$ 
29: end for

```

A.2. Inference and Detection Algorithm

Standard Flow Matching inference involves numerically integrating the learned velocity field v_t^θ from a noise sample x_0 to the data manifold x_1 . Algorithm 2 details this procedure in Diverging Flows. First, we generate the full trajectory $\{\hat{x}_{t_i}\}_{i=0}^N$, typically using Euler integration. Second, we define the ideal transport path as the linear interpolation between the fixed source x_0 and the generated prediction \hat{x}_1 . The anomaly score \hat{S}_{DOT} is computed as the L_1 deviation between the actual neural trajectory and this ideal path, averaged over spatial dimensions and summed over time steps, as defined in Eq. 13. The DOT score depends on the discretized trajectory produced by the numerical ODE solver. In practice, we observe that the relative separation between on- and off-manifold inputs remains stable across reasonable step counts and solver choices, as both valid and invalid trajectories are affected similarly by discretization.

To formulate a binary decision, we compare the calculated score \hat{S}_{DOT} against the conformal interval $[q_{lo}, q_{hi}]$ pre-calibrated on a hold-out set at significance level α . The input condition c is accepted as valid if and only if $\hat{S}_{DOT} \in [q_{lo}, q_{hi}]$; otherwise, the prediction is flagged as an extrapolation.

Algorithm 2 Inference with DOT Scoring using Euler Integrator

```

1: Input: Condition  $c$ , Noise  $x_0 \sim p_0$ , Steps  $N$ 
2: Output: Prediction  $\hat{x}_1$ , Score  $\hat{S}_{DOT}$ 
3: Initialize:
4:  $dt = 1/N$ 
5:  $x = x_0$ 
6:  $\mathcal{X}_{traj} = [x_0]$  ▷ Store trajectory points
7: 1. Generation Loop (Euler)
8: for  $i = 0$  to  $N - 1$  do
9:    $t = i/N$ 
10:  Predict velocity:  $v = v_t^\theta(x, c)$ 
11:  Update state:  $x \leftarrow x + v \cdot dt$ 
12:  Append  $x$  to  $\mathcal{X}_{traj}$ 
13: end for
14: Set prediction:  $\hat{x}_1 = x$ 
15: 2. Calculate  $\hat{S}_{DOT}$ 
16:  $\hat{S}_{DOT} = 0$ 
17: for  $i = 0$  to  $N$  do
18:   Get time:  $t = i/N$ 
19:   Get actual point:  $\hat{x}_t = \mathcal{X}_{traj}[i]$ 
20:   Compute ideal point:  $x_t^{opt} = (1 - t)x_0 + t\hat{x}_1$ 
21:   //Accumulate L1 deviation (averaged over dims D)
22:    $\hat{S}_{DOT} \leftarrow \hat{S}_{DOT} + \frac{1}{D} \sum_{d=1}^D |\hat{x}_t^{(d)} - x_t^{opt,(d)}|$ 
23: end for
24: Return  $\hat{x}_1, \hat{S}_{DOT}$ 

```

B. Experiment Details

B.1. Synthetic Manifold Experiment Details

Data Generation. We utilize the 2D spiral and ambient OOD setup as formally defined in Section 4.1. We strictly enforce a buffer of $\epsilon = 0.025$ between the manifold support and the OOD sampling region to ensure the detection task is unambiguous.

Model Architecture. We employ a time-conditioned Multi-Layer Perceptron (MLP) that processes inputs as flat vectors.

- **Input:** A direct concatenation of the noisy state $x_t \in \mathbb{R}^2$ in the conditional generation task or $x_t \in \mathbb{R}^{20}$ in the regression task, the condition $c \in \mathbb{R}^2$, and the time scalar $t \in [0, 1]$.
- **Backbone:** Three hidden layers of width 512 using SiLU activations.
- **Output:** A linear projection to \mathbb{R}^2 predicting the velocity field u_t .

Training Setup. The model is trained for 20,000 iterations using the AdamW optimizer. Detailed hyperparameters for the architecture and the contrastive loss functions are listed in Table 5.

Note on the Spiral Benchmark. The 2D spiral is a canonical benchmark in the study of Neural ODEs and continuous-time dynamical systems (Chen et al., 2018). Unlike simple shapes, a spiral represents a stiff geometric structure where the optimal transport path (a straight line) often intersects regions that are off-manifold. In the context of probabilistic regression, this experiment is critical because it validates that the learned vector field captures the true non-linear differential equation governing the system’s evolution, rather than memorizing discrete point-to-point mappings. Successfully modeling this dynamics while simultaneously detecting off-manifold perturbations demonstrates that Diverging Flows can enforce safety constraints without over-simplifying the complex curvature of the underlying data manifold.

Table 5. Hyperparameters for Synthetic Manifold Experiments.

Hyperparameter	Conditional Generation	Probabilistic Regression
Hidden Layers	3	3
Hidden Dimension	512	512
Activation	SiLU	SiLU
Optimizer	AdamW	AdamW
Learning Rate	3×10^{-4}	3×10^{-4}
Weight Decay	1×10^{-3}	1×10^{-3}
Batch Size	256	256
Iterations	10,000	20,000
PGD Steps (K)	3	3
Perturbation (η)	0.1	0.1
Repulsion Weight (λ)	0.1	0.1
Curvature Weight (β)	0.05	0.1
Margins (m_r/m_c)	1.0 / 0.9	1.0 / 0.9
Integrator	RK4	RK4
Integration Steps	50	50
Significance Level (α)	0.05	0.05
Target Coverage	95%	95%

B.2. Weather Temperature Forecasting

Dataset. We utilize the ERA5 reanalysis dataset (Hersbach et al., 2020), regressing the surface temperature field six hours into the future. The data is cropped to 64×64 spatial resolution with a single channel (temperature).

Model Architecture. We employ a U-Net backbone modified for conditional generation.

- **Time Conditioning:** The time step $t \in [0, 1]$ is embedded using Fourier features followed by an MLP to produce a 128-dimensional time embedding vector. This embedding is injected into every residual block via FiLM layers.
- **Condition Encoder:** The conditioning input c (current state) is processed by a separate, learnable encoder network. This encoder consists of a convolution followed by 2 residual blocks and 1 downsampling operation.
- **Cross-Attention Injection:** The resulting latent representation from the condition encoder is projected to match the time embedding dimension and injected into the U-Net backbone via cross-attention layers at the 16×16 resolution (lowest level).

Training Setup. We train for 1,000 epochs with a batch size of 64. To ensure stability, we use gradient clipping (norm 1.0) and an Exponential Moving Average (EMA) of model weights with decay 0.9999.

B.3. Cross-Domain Style Transfer Details

Dataset. We perform a cross-domain translation task mapping grayscale MNIST digits ($1 \times 32 \times 32$) to RGB SVHN digits ($3 \times 32 \times 32$).

Model Architecture. We use a U-Net backbone similar to the weather temperature forecasting experiment, but with a stronger dual-conditioning mechanism to preserve high-frequency structural details:

- **Input Concatenation:** Unlike the pure cross-attention approach, here we explicitly concatenate the conditioning image c (1 channel) with the noisy state x_t (3 channels) at the model input, resulting in a 4-channel input tensor. This provides strong spatial guidance for the digit structure.

Table 6. Hyperparameters used in the Weather Temperature Forecasting (ERA5) experiment.

Hyperparameters	
Input Resolution	64×64
Channels	[64, 64, 128]
ResBlocks per Scale	2
Attention Resolution	16×16
Conditioning	Cross-Attention
Time Embedding Dim	128
Optimizer	AdamW
Learning Rate	3×10^{-4}
Weight Decay	1×10^{-2}
AdamW Betas	[0.9, 0.95]
Batch Size	64
EMA Decay	0.9999
Gradient Clip	1.0
PGD Steps (K)	5
Perturbation (η)	0.1
Repulsion Weight (λ)	0.7
Curvature Weight (β)	0.9
Margin m_r	100.0
Margin m_c	0.9
Integrator	Euler
Integration Steps (N)	50
Significance Level (α)	0.05
Target Coverage	95%

- **Cross-Attention:** Additionally, c is processed by a shallow condition encoder (1 ResBlock) and injected via cross-attention at resolutions 16×16 and 8×8 .
- **Backbone:** The U-Net has channel widths of [64, 64, 128] with attention layers at the two lower resolutions.

Training & Inference. The model is trained using AdamW with a learning rate decay schedule. For inference, we employ a 4th-order Runge-Kutta (RK4) integrator with $N = 50$ steps.

B.4. Comparison with DiffPath

For completeness, we provide a reference comparison against DiffPath (Heng et al., 2024), an approach of using diffusion model’s reverse generation path for OOD detection. Unlike our framework, which actively shapes the vector field during training, DiffPath operates as a post-hoc, static detector on a frozen model.

DiffPath usually utilizes a pre-trained model, which is not required to be trained on the in-distribution data. However, due to the lack of pre-trained models for our datasets, we trained a standard Diffusion Model from scratch on the exact in-distribution datasets used in our experiments. DiffPath utilizes this model to perform the reverse generation process on a set of ID calibration samples. It extracts various statistics from these generated trajectories and fits a statistical density estimator (GMM or KDE) to these features. At inference time, the validity of a query input is determined by the likelihood of its trajectory statistics under this fitted distribution.

Table 8 presents the detection performance. While DiffPath serves as an effective external auditor of the generation process, it relies on the assumption that the frozen model will implicitly produce distinguishable trajectory features for OOD inputs. In contrast, Diverging Flows embeds safety directly into the dynamics, ensuring a certified geometric divergence. We observe that our active training approach yields results comparable to this post-hoc analysis.

Table 7. Hyperparameters used in the Style Transfer (MNIST → SVHN) experiment.

Hyperparameters	
Input Resolution	32×32
Channels	[64, 64, 128]
ResBlocks per Scale	2
Attention Resolutions	$16 \times 16, 8 \times 8$
Conditioning	Concat + Cross-Attention
Optimizer	AdamW
Learning Rate	1×10^{-4}
Weight Decay	1×10^{-3}
AdamW Betas	[0.9, 0.95]
Accumulation Steps	4
EMA Decay	0.9999
PGD Steps (K)	5
Perturbation (η)	0.2
Repulsion Weight (λ)	0.1
Curvature Weight (β)	0.7
Margin m_r	10.0
Margin m_c	1.3
Integrator	RK4
Integration Steps (N)	50
Significance Level (α)	0.05
Target Coverage	95%

Table 8. Unified Off-Manifold Detection Performance (AUROC). We report results for the post-hoc detector DiffPath alongside Diverging Flows. Note that we compare only detection capabilities, as DiffPath does not perform the generative prediction task.

Method	Temperature Forecasting		Style Transfer	
	Hotspots		vs FMNIST	vs KMNIST
<i>Post-Hoc Statistics</i>				
DiffPath-1D	0.973		0.981	0.863
DiffPath-6D	0.989		0.991	0.929
<i>Active Training (Ours)</i>				
Diverging Flows (Transformations)	0.733		0.987	0.892
Diverging Flows (PGD)	0.980		0.955	0.860

Remark on Flow vs. Diffusion Dynamics. It is important to note that DiffPath was originally designed for Diffusion Models, which solve a stochastic differential equation (SDE) or its probability flow ODE equivalent. In that regime, the learned vector fields often exhibit complex, non-linear trajectories where OOD inputs *might* induce detectable behavior, such as jittering. However, deploying such passive detectors on Flow Matching models is fundamentally challenging. As discussed in Section 3.3, standard Flow Matching explicitly minimizes transport energy, forcing trajectories to be straight-line geodesics. Due to this strong smoothness bias, unregularized FM models collapse OOD trajectories into efficient, straight paths indistinguishable from valid data. Consequently, passive monitoring of path statistics is often insufficient for Flow Models, necessitating the active geometric regularization introduced in Diverging Flows to explicitly enforce divergence.

C. Visualization of Detection Landscapes

In this section, we visualize the decision boundaries learned by the models within the 2D ambient conditioning space. Figures 5 and 6 depict the landscape of accepted versus rejected conditions.

In these plots, the underlying data manifold is the 2D spiral. The background represents the full ambient space $[-1, 1]^2$. We evaluate the model on a dense grid of conditions; regions highlighted in red indicate conditions flagged as extrapolations (i.e., inputs that trigger a high S_{DST} score).

The results visually confirm the silent failure hypothesis: Standard Flow Matching (left) accepts almost the entire ambient space as valid, driven by its inherent smoothness bias. In contrast, Diverging Flows (right) effectively creates a tight validity boundary that strictly follows the data support, while rejecting the surrounding off-manifold regions (red).

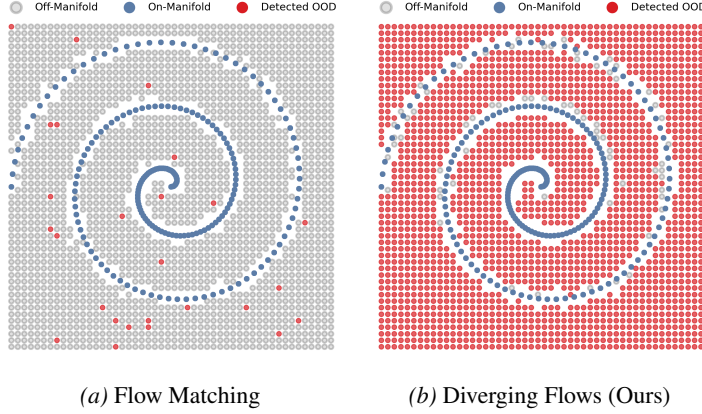


Figure 5. Detection Landscape: Conditional Generation. The standard model (a) fails to distinguish the manifold from the background. Diverging Flows (b) successfully identifies the ambient space as invalid (red), accepting only the spiral support.

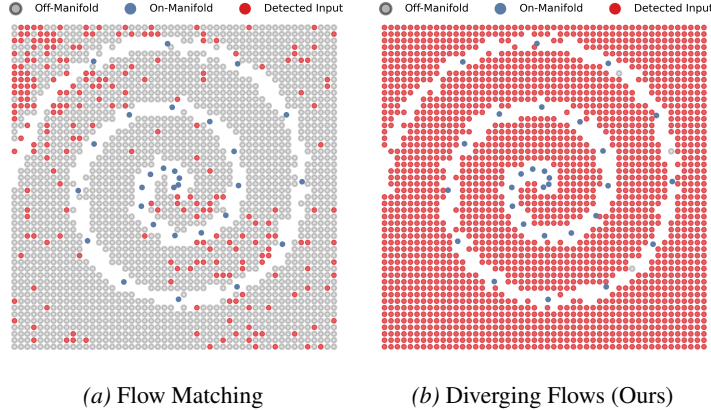


Figure 6. Detection Landscape: Probabilistic Regression. Even in the regression task, where the condition represents a dynamic state x_t , Diverging Flows (b) maintains a precise decision boundary around the valid trajectory path.

D. Extended Conformal Analysis

In the main text, we report the False Positive Rate (FPR) at a fixed error rate $\alpha = 0.05$ (Target Coverage 95%). Here, we expand on the relationship between Target Coverage ($1 - \alpha$) and FPR to characterize detector performance across all operating points.

In Split Conformal Prediction, the True Positive Rate (TPR) is fixed by design to match the target coverage (e.g., setting $\alpha = 0.05$ guarantees valid inputs are accepted 95% of the time). Therefore, the quality of a detector is determined entirely by how few off-manifold samples it accepts at these forced levels of on-manifold acceptance.

- **Ideal Behavior:** An ideal detector perfectly separates on- and off-manifold scores. Consequently, even as we lower the threshold to accept 99% of on-manifold data, the FPR should remain near 0%.
- **Random Guessing (Baseline):** If the on and off-manifold score distributions overlap perfectly (as seen with standard Flow Matching), accepting $X\%$ of the on-manifold volume statistically necessitates accepting $\approx X\%$ of the OOD volume. This results in a diagonal line where $\text{FPR} \approx \text{Coverage}$.

Our results show that Diverging Flows maintains an $\text{FPR} < 10\%$ even as Target Coverage approaches 95%, whereas the baseline FPR rises linearly with coverage. This confirms that our geometric score provides a high-margin separation, allowing for safe deployment even at strict recall requirements.

E. Additional Qualitative Results

In this section, we provide weather temperature forecasting (Figure 8) and style transfer (Figure 7) samples from Diverging Flows.

Style Transfer (MNIST \rightarrow SVHN) Examples



Figure 7. Extended Style Transfer Samples. Pairs of Conditioning Inputs (MNIST) and Generated Outputs (SVHN). The model successfully maps the sparse structural guidance of the grayscale digit to the rich, multi-modal distribution of street view imagery.

Diverging Flows Weather Forecasts

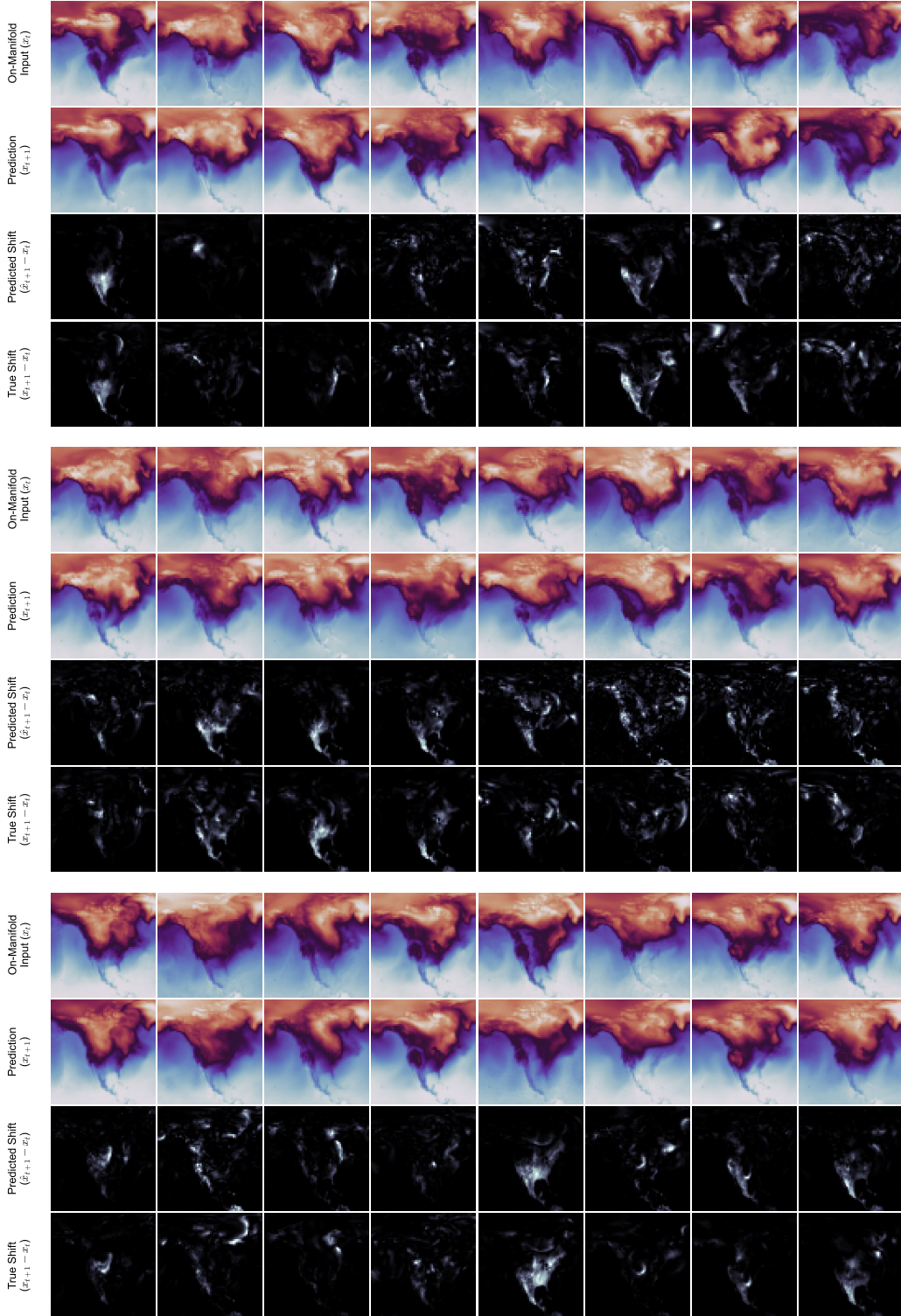


Figure 8. Extended Weather Temperature Forecasting Samples. Randomly selected 6-hour temperature forecasts generated by Diverging Flows on the ERA5 validation set. The model generates physically consistent heatmaps that align with the ground truth dynamics.